Editors' Suggestion

Interferometric Readout of Momentum-Space Topology in a Programmable Dissipative Photonic Circuit

Andrea Cataldo,[1,*] Emil J. Bergholtz,[2] Daniel Leykam,[3] Jun Gao,[4,5,6,†] and Ali W. Elshaari[1,‡]
[1]Department of Applied Physics, KTH Royal Institute of Technology, Albanova University Centre, Roslagstullsbacken 21, 106 91 Stockholm, Sweden
[2]Department of Physics, Stockholm University, 106 91 Stockholm, Sweden
[3]Singapore University of Technology and Design, 8 Somapah Road, 487372 Singapore, Singapore
[4]School of Optical and Electronic Information, Huazhong University of Science and Technology, Wuhan 430074, China
[5]Research Center for Cross-Scale Global-Scale Multimodal Optical Communication Discipline and Technology, Wuhan 430074, China
[6]Optics Valley Laboratory, 1037 Luoyu Road, Wuhan 430074, People's Republic of China

(Received 24 May 2026; revised 24 September 2026; accepted 28 September 2026; published 12 November 2026)

Topology under non-Hermitian dynamics is encoded in the phase of the bulk evolution, yet strong dissipation suppresses the amplitudes carrying it. We resolve this using a programmable photonic integrated circuit that implements such dynamics in synthetic momentum space through unitary dilation, with the phase recovered by phase-shifted interferometry. For the non-Hermitian Su-Schrieffer-Heeger model, the method distinguishes trivial and nontrivial Zak phases and yields a coherence winding $q = \pm 1$ induced by an exceptional point. Extending to a synthetic torus via a Rice-Mele pump gives the first Chern number $\mathrm{Ch}_1 = 0, 1$ for trivial and nontrivial cycles, showing a programmable route to momentum-space topology under strongly dissipative non-Hermitian dynamics.

DOI: 10.1103/xkht-64kc

Topology in condensed matter and photonics is most naturally expressed in momentum space, where invariants such as the Zak phase, Chern number, and winding numbers are defined directly on the Brillouin zone. In photonic platforms, however, these invariants are most often inferred indirectly, through their bulk-boundary correspondence as edge or interface states [1–3]. While such boundary signatures have established the field, they probe topology only through its consequences rather than its momentum-space origin, and they require finite, carefully terminated structures in which edge modes are well separated from the bulk. A complementary line of work has therefore sought to probe bulk invariants directly through the dynamics of wave packets in real-space lattices. These dynamical approaches reach quantities ranging from Zak phases in chiral and nonchiral one-dimensional models [4–9] to non-Hermitian topological transitions [10–12] and topological invariants under loss [13]. The invariant is often obtained as a bulk-averaged quantity, as in the mean chiral displacement, which converges at long times [14]. They nonetheless inherit the limitations of finite real-space implementations: discrete momentum sampling set by the lattice extent, sensitivity to

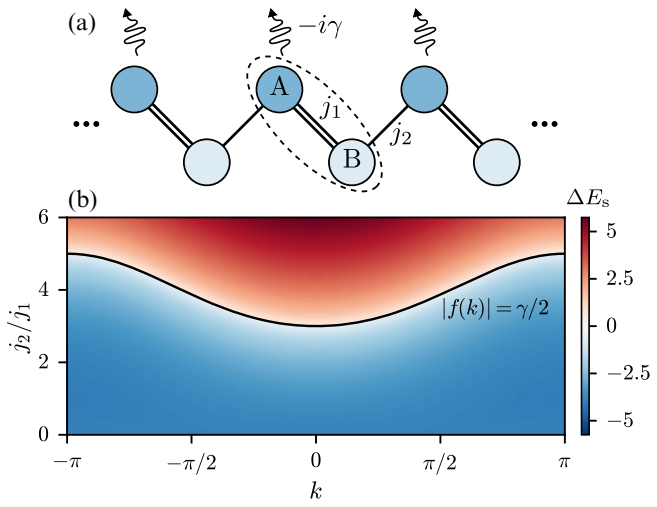


FIG. 1. (a) Real-space representation of the non-Hermitian Su-Schrieffer-Heeger (SSH) lattice, with intracell and intercell couplings j_1 and j_2, respectively, and loss $-i\gamma$ on the A sites. The dashed ellipse marks the (A, B) unit cell. (b) Momentum-space band splitting ΔE_s, piecewise defined by $\Delta E_s = \mathrm{Re}(E_+ - E_-)$ for $|f(k)| \geq \gamma/2$ and $\Delta E_s = -\mathrm{Im}(E_+ - E_-)$ for $|f(k)| < \gamma/2$, shown in the $(k, j_2/j_1)$ plane for $j_1 = 0.5$ and $\gamma = 4$. The black curve marks the exceptional point (EP) condition $|f(k)| = \gamma/2$.

*Contact author: andreacl@kth.se
†Contact author: jungao@hust.edu.cn
‡Contact author: elshaari@kth.se

Published by the American Physical Society under the terms of the Creative Commons Attribution 4.0 International license. Further distribution of this work must maintain attribution to the author(s) and the published article's title, journal citation, and DOI. Funded by Bibsam.

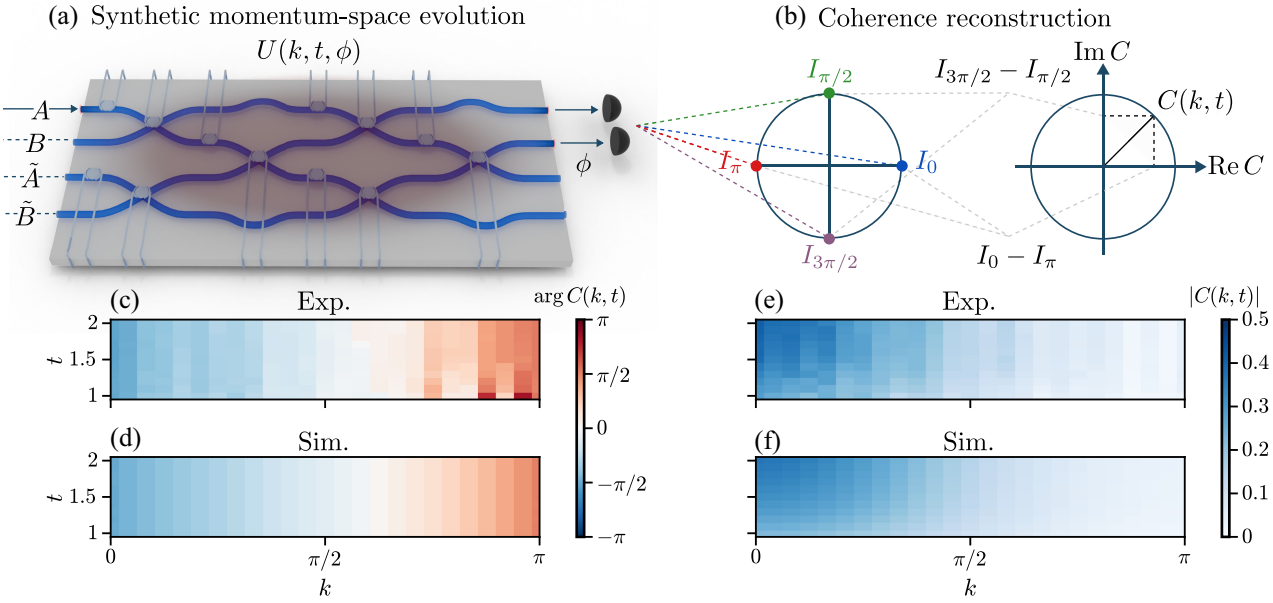


FIG. 2. (a) Schematic of the interferometric readout for synthetic momentum-space evolution on a programmable photonic integrated circuit (PIC). Light is launched into spatial mode A, with (A, B) spanning the signal subspace and $(\tilde{A}, \tilde{B})$ spanning the ancilla subspace. The PIC implements a compiled 4×4 transformation $U(k,t,\phi) = U_{\mathrm{int}}(\phi)U_{\mathrm{dil}}(k,t)$, which combines the dilation and phase-shifted interferometric readout. Two quadratures are formed as shown in (b), allowing for reconstruction of the coherence $C(k,t)$ as in Eq. (2). For the parameters $j_1 = 0.5$, $j_2 = 1.5$, and $\gamma = 4$, the relative phase $\arg C(k,t)$ is obtained for the experiment (c) and simulation (d), with (e) and (f) showing the corresponding magnitude $|C(k,t)|$. All data are shown for a representative well-conditioned interval $t \in [1,2]$, with $N_k = 25$ uniformly spaced momentum points over $k \in [0,\pi]$. The root-mean-square errors (RMSEs) relative to simulation are 0.0613π for the phase and 0.0194 for the magnitude.

finite-size and boundary effects, and limited reconfigurability once the device is fabricated.

In parallel, grating-based, metasurface, and photonic-crystal systems have provided more direct momentum-space access, with topological invariants extracted from reflection or far-field radiation in one-dimensional photonic crystals and metasurfaces [15–17] and from non-Hermitian guided-mode resonances at nanophotonic interfaces [18]. These approaches yield clean spectroscopic signatures but are tied to fixed geometries, so scanning across the parameter space of a topological model requires fabricating a new sample. These considerations motivate a complementary route that combines the direct momentum-space access of these spectroscopic platforms with the reconfigurability needed to traverse topological phase diagrams and that remains viable in the strongly dissipative regime where non-Hermitian physics is richest [19,20]. Strong dissipation is particularly demanding because it suppresses the evolved amplitudes whose relative phase carries the topological information.

Here, a programmable photonic integrated circuit (PIC) [21,22] is used to simulate non-Hermitian dynamics directly in synthetic momentum space, with each momentum point realized as a separately programmed unitary on the same hardware. Such pointwise access differs from a synthetic dimension formed by dynamically coupled modes [23]. The method requires neither a real-space boundary nor spectrally resolved edge modes. The experimental implementation builds on the platform of Ref. [24]. Strong dissipation is handled by embedding the nonunitary evolution into a larger unitary via Sz.-Nagy dilation [25]—an approach also used to realize non-Hermitian dynamics on spin and superconducting platforms [26,27]—while the phase of the evolved signal is recovered through phase-shifted interferometric readout. The method is first demonstrated in the non-Hermitian Su-Schrieffer-Heeger (SSH) model, where it extracts the Zak phase and reveals an interferometric signature of an exceptional point (EP), before being extended to a higher-dimensional synthetic space through the first Chern number of a non-Hermitian Rice-Mele pump.

The model is shown in Fig. 1(a), and its momentum-space Hamiltonian reads as

$$H(k) = \begin{bmatrix} -i\gamma & f(k) \\ f^*(k) & 0 \end{bmatrix}, \qquad f(k) = j_1 + j_2 e^{-ik}, \quad (1)$$

where j_1 and j_2 denote the intracell and intercell couplings, respectively. The coupling function $f(k)$ traces a trajectory in the $(\mathrm{Re}f, \mathrm{Im}f)$ plane that determines the winding and hence the topology. A loss term $-i\gamma$ is included directly in $H(k)$, so for $|f(k)| < \gamma/2$ the dynamics lies in the dissipative regime; there, the two bands are distinguished not by $\mathrm{Re}E_\pm(k)$ but by $\mathrm{Im}\,E_\pm(k)$, i.e., by their decay rates, as shown in Fig. 1(b).

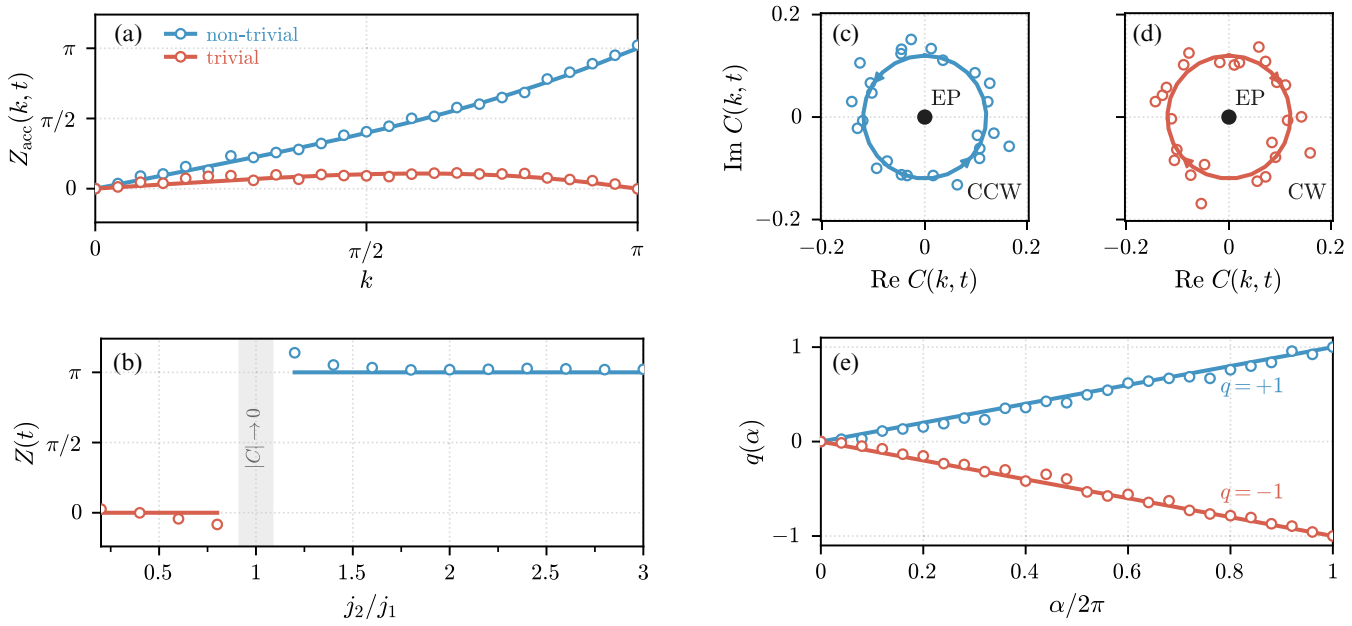


FIG. 3. Extraction of momentum-space topology. (a) Accumulated Zak phase $Z_{\mathrm{acc}}(k,t)$, as defined by Eq. (3), for the nontrivial and trivial cases, corresponding to $(j_1, j_2, \gamma) = (0.5, 1.5, 4)$ and $(1.5, 0.5, 4)$, respectively. Circles denote experiment, and lines denote the simulation. The extracted values at $k = \pi$ are 1.02π and -0.00148π. (b) Zak phase $Z(t)$ versus j_2/j_1 for fixed $j_1 = 0.5$, showing quantization to 0 and π, with average values of -0.0254π and 1.04π on the two sides of the transition. A shaded region near the transition indicates $|C| \to 0$. (a),(b) For $t = 2$, with $N_k = 25$ uniformly spaced momentum points over $k \in [0, \pi]$, i.e., 100 unitaries per parameter set. (c),(d) Encirclement of an EP-induced coherence zero using the same circular contour with reversed traversal, counterclockwise (CCW) and clockwise (CW). Circles denote the measured $C(k,t)$, and lines denote the simulation. (e) EP-induced coherence winding $q(\alpha)$ versus $\alpha/2\pi$, obtained by integrating according to Eq. (4). Both simulation and experiment give $q = 1$ for CCW and $q = -1$ for CW.

For each k, the evolution over time t is described by the propagator $e^{-iH(k)t}$. Because the PIC natively implements unitary transformations, this propagator is rescaled by its largest singular value to become a contraction, and is thereby dilated to a Sz.-Nagy unitary $U_{\mathrm{dil}}(k,t)$. The target evolution then acts on the (A, B) signal subspace of the SSH model, while $(\tilde{A}, \tilde{B})$ provide the ancilla subspace that makes the unitary realization possible, as shown in Fig. 2(a) and detailed in Supplemental Material [28].

The evolved (A, B) signal amplitudes are then subjected to interferometric readout through $U_{\mathrm{int}}(\phi)$, which mixes them against four phase-shifted references at $\phi = 0, \pi/2, \pi$, and $3\pi/2$. These readings provide the phase quadratures [30], shown in Fig. 2(b), from which one forms the interferometric coherence,

$$C(k,t) = [I_0 - I_\pi] + i[I_{3\pi/2} - I_{\pi/2}], \tag{2}$$

where I_ϕ denotes the output intensity at phase reference ϕ, with the (k,t) dependence omitted for brevity. The phase $\arg C(k,t)$ gives the relative phase of the A and B amplitudes, while $|C(k,t)|$ sets the strength of the readout.

An example of this interferometric readout is shown in Figs. 2(c)–2(f) for the nontrivial case with $j_1 = 0.5$, $j_2 = 1.5$, and $\gamma = 4$. The measured phase readout reproduces the main features of the corresponding simulation. Deviations occur mainly in regions of diminished coherence. This is because, as $|C(k,t)|$ becomes small, the phase becomes increasingly ill conditioned. In such cases this may produce abrupt phase variations, but away from these regions the phase varies smoothly.

These deviations should not be confused with generic disorder in a real-space lattice, which would break translational symmetry and couple different momenta. Indeed, the finite fidelity of the programmed unitary is the relevant experimental imperfection. It can be mitigated by using a calibrated model of an imperfect PIC [31–33] that accounts for the actual device response [28].

By repeating the readout at successive k-points, one traces the phase across the BZ. For the chosen input state, $\partial_k \arg C = \partial_k \arg f^*(k)$ [28]. This in turn provides access to the Zak phase, here that of the Hermitian parent model, with its accumulation defined by

$$Z_{\mathrm{acc}}(k,t) = \int_0^k dk' \partial_{k'} \arg C(k',t). \tag{3}$$

Figure 3(a) shows $Z_{\mathrm{acc}}(k,t)$ for the nontrivial and trivial cases. In the nontrivial case, it increases progressively with k and reaches nearly π at the boundary, consistent with a net winding. In the trivial case, it shows only a small excursion and returns nearly to zero at the end, indicating vanishing net winding. This behavior is consistent with the

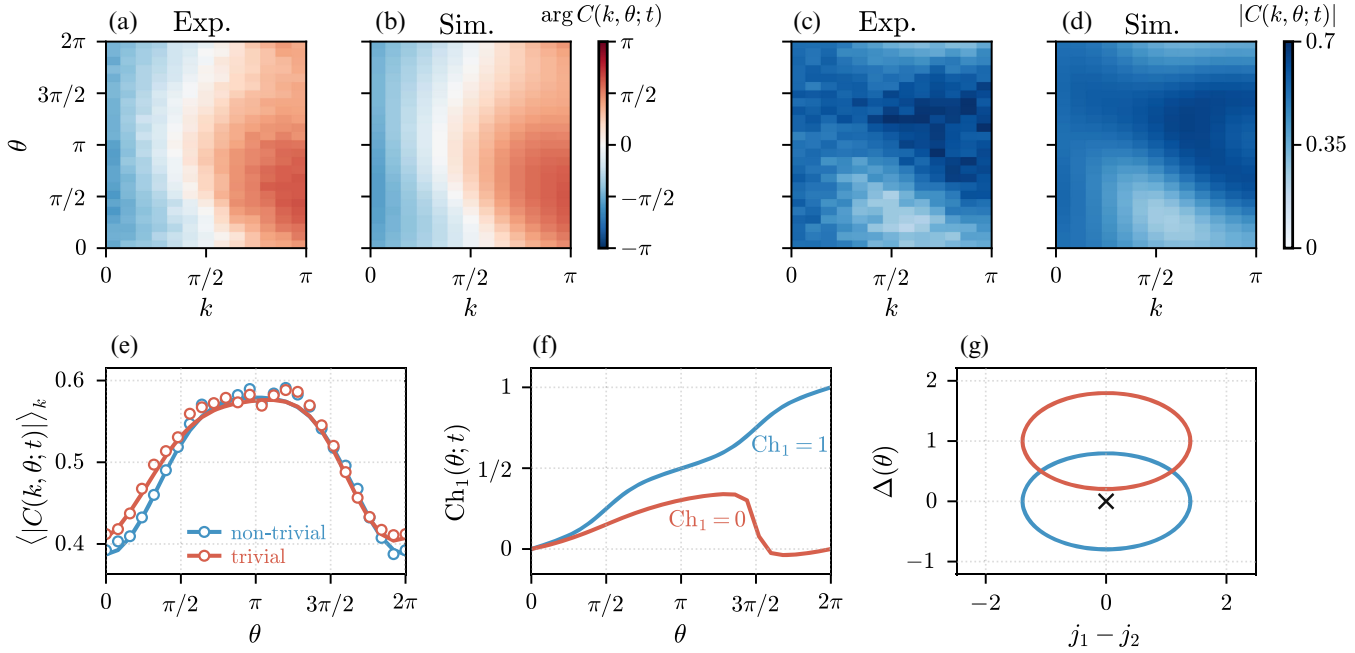


FIG. 4. Higher-dimensional synthetic space extension of a non-Hermitian Rice-Mele pump. (a)–(d) Reconstructed coherence of the nontrivial pump cycle with $(j_0, \delta, \Delta_c, \Delta_0, \gamma, t) = (2, 0.7, 0, 0.8, 2, 0.25)$, shown as phase and magnitude for experiment and simulation. The input state is $(1, -i)^T/\sqrt{2}$, giving RMSEs relative to simulation of 0.0208π and 0.0302, respectively. (e) Momentum-averaged magnitude $\langle|C(k, \theta; t)|\rangle_k$ for nontrivial and trivial pump cycles. Lines denote simulation, and circles denote experiment; the RMSEs of the averaged traces are 0.00769 and 0.00864, respectively. (f) Accumulated first Chern number inferred from the experimentally reconstructed pump trajectory, giving $\mathrm{Ch}_1 = 1$ and $\mathrm{Ch}_1 = 0$ for the nontrivial and trivial cycles, respectively. (g) Pump cycles in the $(j_1 - j_2, \Delta)$ plane relative to the gap closing (cross), with the trivial cycle shifted upward by $\Delta_c = 1$, so only the nontrivial cycle encloses it. The fitted cycles preserve this separation, with margins 0.805 (nontrivial) and 0.175 (trivial) from the gap closing, which keeps the Chern number extraction in (f) stable. All data use $N_k = N_\theta = 25$ uniformly spaced points over $k, \theta \in [0, 2\pi)$, i.e., 2500 unitaries per cycle; (a)–(d) show only $k \in [0, \pi]$, over which their quoted RMSEs are evaluated.

underlying model, where $f(k)$ encloses the origin in the former case but does not in the latter. The distinction of topology is thus already evident throughout the accumulated phase trace. The same distinction is seen in Fig. 3(b), which plots the Zak phase $Z(t) = Z_{\mathrm{acc}}(\pi, t)$ against j_2/j_1 for fixed $j_1 = 0.5$. There, the measured values lie near 0 for $j_2/j_1 < 1$ and near π for $j_2/j_1 > 1$.

One may also probe the interferometric signature of the EP itself. The accumulated phase is evaluated along a closed contour in the $(\mathrm{Re}C, \mathrm{Im}\,C)$ plane. An EP-induced coherence winding can be obtained by

$$q(\alpha) = \frac{1}{2\pi} \int_{\mathcal{L}(\alpha)} d \arg C(k, t), \tag{4}$$

where $\mathcal{L}(\alpha)$ is this contour traced up to α. In the coherence plane, the EP manifests itself as the point $C(k, t) = 0$. Therefore, a convenient choice is to take the contour as a circle within this plane, so $|C(k, t)|$ is kept finite. This is visualized in Figs. 3(c) and 3(d) for two orientations of the same contour. The resulting $q(\alpha)$ progresses linearly, with opposite windings $q = \pm 1$, as seen in Fig. 3(e). We emphasize that q as defined in Eq. (4) is distinct from the conventional eigenvalue vorticity associated with a second-order EP, which arises from the branch-point structure and yields a half-integer winding $\pm 1/2$ upon encircling the EP in parameter space. By contrast, q counts the integer winding of $\arg C(k, t)$ around the zero of the interferometric coherence induced by the EP. This provides a complementary characterization of the EP, based on the phase imprinted on the experimentally accessible coherence signal rather than on direct observation of the eigenvalue spectrum.

As an extension to higher-dimensional synthetic space, consider the non-Hermitian Rice-Mele model with a pump parameter $\theta \in [0, 2\pi)$, so (k, θ) spans a synthetic torus. The Hamiltonian reads as

$$H_{\mathrm{RM}}(k, \theta) = \begin{bmatrix} \Delta(\theta) - i\gamma & f(k, \theta) \\ f^*(k, \theta) & -\Delta(\theta) \end{bmatrix}, \tag{5}$$

where $f(k, \theta) = j_1(\theta) + j_2(\theta) e^{-ik}$, $j_{1,2}(\theta) = j_0 \pm \delta \cos\theta$, and $\Delta(\theta) = \Delta_c + \Delta_0 \sin\theta$. Over one pump cycle, the associated first Chern number can then be obtained from the winding of the Zak phase as [34]

$$\mathrm{Ch}_1 = \frac{1}{2\pi}\int_0^{2\pi} d\theta\, \partial_\theta Z(\theta). \tag{6}$$

The coherence now becomes $C(k,\theta;t)$ and is determined using the same interferometric method, with its phase and magnitude shown for nontrivial pumping in Figs. 4(a)–4(d). The experiment follows closely with the simulation; indeed, the momentum-averaged magnitude $\langle|C(k,\theta;t)|\rangle_k$ stays clearly resolved for both cycles, well above the low-coherence regime, as seen in Fig. 4(e).

This measured coherence is then used to infer the pump trajectory. A candidate Rice-Mele loop is specified in the $(j_1 - j_2, \Delta)$ plane, from which the expected coherence is computed and compared with the measured one. A fit of these quantities gives the invariant shown in Fig. 4(f), taking the values $\mathrm{Ch}_1 = 0, 1$ for the trivial and nontrivial cycles, respectively. This is consistent with whether the corresponding Rice-Mele loop misses or encloses the gap closing in Fig. 4(g). For the chosen parameters, these fitted loops remain well separated from the gap closing, so small readout errors only deform the pump trajectories without changing their winding.

In conclusion, we have demonstrated direct interferometric readout of non-Hermitian topological invariants in synthetic momentum space, resolving the central experimental challenge that strong dissipation suppresses the amplitudes carrying the topological phase. The method proceeds by (i) implementing the dilated evolution, (ii) reconstructing the coherence from four phase-shifted intensity measurements, and (iii) extracting the corresponding topological invariant from this coherence. From this readout, the Zak phase and an EP-induced coherence winding of the SSH model, together with the first Chern number of a Rice-Mele pump, are obtained, thereby demonstrating a programmable route to higher-dimensional momentum-space topology in photonics. An N-band model requires N signal and N ancillary modes [28]. The reconfigurability of the platform makes it naturally suited to the experimental investigation of non-Hermitian symmetry classes and topological invariants that remain inaccessible to fixed-geometry platforms.

Acknowledgments—A. C. and A. W. E. acknowledges the support from the Knut and Alice Wallenberg (KAW) Foundation through the Wallenberg Centre for Quantum Technology (WACQT). E. J. B. acknowledges the support from the Knut and Alice Wallenberg Foundation under Grant No. 2023.0256 and the Göran Gustafsson Foundation for Research in Natural Sciences and Medicine. D. L. acknowledges support from the Ministry of Education, Singapore, under its SUTD Kickstarter Initiative under Grant No. SKI 20210501. J. G. acknowledges support from Swedish Research Council under Grants No. 2023-06671 and No. 2023-05288, the Vinnova Project No. 2024-00466, and the Göran Gustafsson Foundation. A. W. E acknowledges support from Swedish Research Council (VR) Starting Grant No. 2016-03905 and the Vinnova Quantum Kick-Start Project 2021.

Data availability—There are no publicly available research data or software supporting this manuscript. Requests for further information or data should be sent to the authors.

[1] M. Hafezi, S. Mittal, J. Fan, A. Migdall, and J. M. Taylor, Imaging topological edge states in silicon photonics, Nat. Photonics **7**, 1001 (2013).
[2] Jiho Noh, Sheng Huang, Kevin P. Chen, and Mikael C. Rechtsman, Observation of photonic topological valley Hall edge states, Phys. Rev. Lett. **120**, 063902 (2018).
[3] Tomoki Ozawa, Hannah M. Price, Alberto Amo, Nathan Goldman, Mohammad Hafezi, Ling Lu, Mikael C. Rechtsman, David Schuster, Jonathan Simon, Oded Zilberberg, and Iacopo Carusotto, Topological photonics, Rev. Mod. Phys. **91**, 015006 (2019).
[4] Filippo Cardano, Alessio D'Errico, Alexandre Dauphin, Maria Maffei, Bruno Piccirillo, Corrado De Lisio, Giulio De Filippis, Vittorio Cataudella, Enrico Santamato, Lorenzo Marrucci, Maciej Lewenstein, and Pietro Massignan, Detection of Zak phases and topological invariants in a chiral quantum walk of twisted photons, Nat. Commun. **8**, 15516 (2017).
[5] S. Longhi, Probing one-dimensional topological phases in waveguide lattices with broken chiral symmetry, Opt. Lett. **43**, 4639 (2018).
[6] Stefano Longhi, Probing topological phases in waveguide superlattices, Opt. Lett. **44**, 2530 (2019).
[7] Yao Wang, Yong-Heng Lu, Feng Mei, Jun Gao, Zhan-Ming Li, Hao Tang, Shi-Liang Zhu, Suotang Jia, and Xian-Min Jin, Direct observation of topology from single-photon dynamics, Phys. Rev. Lett. **122**, 193903 (2019).
[8] Zhi-Qiang Jiao, Stefano Longhi, Xiao-Wei Wang, Jun Gao, Wen-Hao Zhou, Yao Wang, Yu-Xuan Fu, Li Wang, Ruo-Jing Ren, Lu-Feng Qiao, and Xian-Min Jin, Experimentally detecting quantized Zak phases without chiral symmetry in photonic lattices, Phys. Rev. Lett. **127**, 147401 (2021).
[9] Ze-Sheng Xu, Jun Gao, Govind Krishna, Stephan Steinhauer, Val Zwiller, and Ali W. Elshaari, Direct measurement of topological invariants in photonic superlattices, Photonics Res. **10**, 2901 (2022).
[10] Julia M. Zeuner, Mikael C. Rechtsman, Yonatan Plotnik, Yaakov Lumer, Stefan Nolte, Mark S. Rudner, Mordechai Segev, and Alexander Szameit, Observation of a topological transition in the bulk of a non-Hermitian system, Phys. Rev. Lett. **115**, 040402 (2015).
[11] Shunyu Yao and Zhong Wang, Edge states and topological invariants of non-Hermitian systems, Phys. Rev. Lett. **121**, 086803 (2018).
[12] Flore K. Kunst, Elisabet Edvardsson, Jan Carl Budich, and Emil J. Bergholtz, Biorthogonal bulk-boundary correspondence in non-Hermitian systems, Phys. Rev. Lett. **121**, 026808 (2018).

[13] Daniel Leykam and Daria A. Smirnova, Probing bulk topological invariants using leaky photonic lattices, Nat. Phys. **17**, 632 (2021).
[14] Maria Maffei, Alexandre Dauphin, Filippo Cardano, Maciej Lewenstein, and Pietro Massignan, Topological characterization of chiral models through their long time dynamics, New J. Phys. **20**, 013023 (2018).
[15] Wen Sheng Gao, Meng Xiao, C. T. Chan, and Wing Yim Tam, Determination of Zak phase by reflection phase in 1D photonic crystals, Opt. Lett. **40**, 5259 (2015).
[16] Maxim A. Gorlach, Xiang Ni, Daria A. Smirnova, Dmitry Korobkin, Dmitry Zhirihin, Alexey P. Slobozhanyuk, Pavel A. Belov, Andrea Alù, and Alexander B. Khanikaev, Far-field probing of leaky topological states in all-dielectric metasurfaces, Nat. Commun. **9**, 909 (2018).
[17] C. Liu, H. R. Wang, and H. C. Ong, Determination of the Zak phase of one-dimensional diffractive systems with inversion symmetry via radiation in Fourier space, Phys. Rev. B **108**, 035403 (2023).
[18] Ki Young Lee, Kwang Wook Yoo, Youngsun Choi, Gunpyo Kim, Sangmo Cheon, Jae Woong Yoon, and Seok Ho Song, Topological guided-mode resonances at non-Hermitian nanophotonic interfaces, Nanophotonics **10**, 1853 (2021).
[19] Ramy El-Ganainy, Konstantinos G. Makris, Mercedeh Khajavikhan, Ziad H. Musslimani, Stefan Rotter, and Demetrios N. Christodoulides, Non-Hermitian physics and PT symmetry, Nat. Phys. **14**, 11 (2018).
[20] Emil J. Bergholtz, Jan Carl Budich, and Flore K. Kunst, Exceptional topology of non-Hermitian systems, Rev. Mod. Phys. **93**, 015005 (2021).
[21] Wim Bogaerts, Daniel Pérez, José Capmany, David A. B. Miller, Joyce Poon, Dirk Englund, Francesco Morichetti, and Andrea Melloni, Programmable photonic circuits, Nature (London) **586**, 207 (2020).
[22] Mehmet Berkay On, Farshid Ashtiani, David Sanchez-Jacome, Daniel Perez-Lopez, S. J. Ben Yoo, and Andrea Blanco-Redondo, Programmable integrated photonics for topological Hamiltonians, Nat. Commun. **15**, 629 (2024).
[23] Shirong Lin, Luojia Wang, Luqi Yuan, and Xianfeng Chen, All-optical control of the photonic Hall lattice in a pumped waveguide array, Phys. Rev. Appl. **17**, 064029 (2022).
[24] Ze-Sheng Xu, J. Lukas K. König, Andrea Cataldo, Rohan Yadgirkar, Govind Krishna, Venkatesh Deenadayalan, Val Zwiller, Stefan Preble, Emil J. Bergholtz, Jun Gao, and Ali W. Elshaari, Non-Hermitian exceptional topology on a Klein bottle photonic circuit, Light: Sci. Appl. **15**, 390 (2026).
[25] Zixuan Hu, Rongxin Xia, and Sabre Kais, A quantum algorithm for evolving open quantum dynamics on quantum computing devices, Sci. Rep. **10**, 3301 (2020).
[26] Yang Wu, Wenquan Liu, Jianpei Geng, Xingrui Song, Xiangyu Ye, Chang-Kui Duan, Xing Rong, and Jiangfeng Du, Observation of parity-time symmetry breaking in a single-spin system, Science **364**, 878 (2019).
[27] Shruti Dogra, Artem A. Melnikov, and Gheorghe Sorin Paraoanu, Quantum simulation of parity–time symmetry breaking with a superconducting quantum processor, Commun. Phys. **4**, 26 (2021).
[28] See Supplemental Material at http://link.aps.org/supplemental/10.1103/xkht-64kc for supporting theory and methodological details, which includes Ref. [29].
[29] William R. Clements, Peter C. Humphreys, Benjamin J. Metcalf, W. Steven Kolthammer, and Ian A. Walmsley, Optimal design for universal multiport interferometers, Optica **3**, 1460 (2016).
[30] P. Hariharan, *Optical Interferometry*, 2nd ed. (Elsevier Academic Press, Amsterdam, 2003).
[31] Andreas Fyrillas, Olivier Faure, Nicolas Maring, Jean Senellart, and Nadia Belabas, Scalable machine learning-assisted clear-box characterization for optimally controlled photonic circuits, Optica **11**, 427 (2024).
[32] Jin-Hao Zheng, Qin-Qin Wang, Lan-Tian Feng, Yu-Yang Ding, Xiao-Ye Xu, Xi-Feng Ren, Chuan-Feng Li, and Guang-Can Guo, Global calibration of large-scale photonic integrated circuits, Phys. Rev. Appl. **22**, 054011 (2024).
[33] ZeYang Fan, JunMin Lin, Tian Zhang, Jian Dai, XingYuan Xu, and Kun Xu, Efficient off-chip configuration method for scalable programmable photonic integrated circuits, Commun. Phys. **8**, 218 (2025).
[34] D. J. Thouless, Quantization of particle transport, Phys. Rev. B **27**, 6083 (1983).